FINAL REPORT

ON

NASA GRANT NAG8-185

TO

THE MASSACHUSETTS INSTITUTE OF TECHNOLOGY

FOR

DETERMINATION OF THE ATMOSPHERIC STRUCTURE OF THE BO STAR COMPANION OF SMC X-1 BY ANALYSIS OF GINGA OBSERVATIONS

submitted by

Principal Investigator: George W. Clark
November 8, 1994

Observations of SMC X-1 were made from 1989 July 29 to August 3 with the LAC gas proportional counters of the Ginga X-ray observatory as requested in the proposal for the project supported by this grant. Analysis of the resulting data by the principal investigator and Jonathan Woo, supplemented by a study of high-resolution imaging data from the ROSAT X-ray observatory and 3-D numerical hydrodynamical simulations carried out by Jon Blondin of the North Carolina State University in collaboration with Jonathan Woo, resulted in a variety of conclusions regarding the atmospheric structure of the companion of SMC X-1. Of special interest are the results bearing on the influence of high-intensity X-ray illumination on the propagation of the stellar wind and the action of the radiation driving force.

A paper entitled "Wind Dynamics in SMC X-1: II. Ginga and Rosat Observations" and a companion paper entitled "Wind Dynamics in SMC X-1: I. Hydrodynamic Simulation" by Blondin and Woo have been accepted for publication in the Astrophysical Journal and will appear during 1995. A copy of the first manuscript, based on the effort supported by GRANT NAG8-185, is attached to this report.

Wind Dynamics in SMC X-1:
II. *Ginga* and *ROSAT* Observations

Jonathan W. Woo and George W. Clark[1]

Center for Space Research, Massachusetts Institute of Technology, Cambridge, MA 02139

John M. Blondin

Department of Physics, North Carolina State University, Raleigh, NC 27695-8202

Timothy R. Kallman

Laboratory for High Energy Astrophysics, NASA/Goddard Space Flight Center,

Greenbelt, MD 20771

and

Fumiaki Nagase

The Institute of Space and Astronautical Science, 3-1-1 Yoshinodai, Sagamihara,

Kanagawa 229, Japan

---

[1]Department of Physics, Massachusetts Institute of Technology, Cambridge, MA 02139

ABSTRACT

The X-ray phenomena of the binary system SMC X-1/Sk 160, observed with the *Ginga* and *ROSAT* X-ray observatories, are compared with computed phenomena derived from a 3D hydrodynamical model of the stellar wind perturbed by X-ray heating and ionization which is described in the accompanying paper (Blondin & Woo 1994). In the model the B0I primary star has a line-driven stellar wind in the region of the X-ray shadow and a thermal wind in the region heated by X-rays. We find general agreement between the observed and predicted X-ray spectra throughout the binary orbit cycle, including the extended, variable, and asymmetric eclipse transitions and the period of deep eclipse.

Subject headings: Binaries: Eclipsing — Stars: Circumstellar Matter — Stars: Mass Loss — Pulsars: Individual (SMC X-1) — X-Rays: Stars

1. INTRODUCTION

Information about the distribution of matter around an X-ray binary can be inferred from observations of the variations with orbital phase of its X-ray spectrum caused by absorption along the line of sight to the X-ray star. The eclipse transition phenomena of a high mass X-ray binary (HMXB), in particular, provide a unique opportunity to explore the atmospheric structure of the primary star which is generally an early-type giant or supergiant with an intense, line-driven stellar wind. However, the X-ray luminosity, if sufficiently high, can cause complications by disrupting the flow of the line-driven stellar wind and modifying the X-ray absorption cross sections. An extreme example of such a situation is the ultra-luminous binary X-ray pulsar SMC X-1/Sk 160. In this paper we describe the X-ray phenomena of this binary system as observed by *Ginga* during 1.3 orbit cycles, including two eclipsed periods with one eclipse ingress and two egresses. We show that the observed variations of the X-ray spectrum and intensity match the expected effects of absorption and scattering by matter distributed in the pattern derived in the 3D hydrodynamical model developed by Blondin & Woo (1994; hereafter Paper I).

Properties of the stellar winds of the primary stars in eclipsing HMXBs have been inferred from X-ray observations in numerous investigations, e. g., Cen X-3 by Schreier et al. (1976), Clark, Minato, & Mi (1988), Day & Stevens (1993); 4U 1700-37 by Haberl, White, & Kallman (1989) and Heap & Corcoran (1992); Vela X-1 by Sato et al. (1986), Lewis et al. (1992); 4U 1538-52 by Clark, Woo, & Nagase (1994). All of these investigations, except that of Haberl et al. (1989) and Heap & Corcoran (1992), have found that the average run of atmospheric density in the subsonic region close to the stellar surfaces can be represented as an exponential function of radius with a scale height of the order of 1/20 of the stellar radius. Such representations differ in form from the density functions derived in steady-state theories of line-driven winds (e.g., Castor, Abbott, & Klein 1975), which

tend to produce eclipse transitions that are more abrupt than observations indicate. The derived exponential function might, perhaps, represent an average over inherently turbulent subsonic flows like those explored in time-dependent hydrodynamic simulations, e. g., Poe, Owocki, & Castor (1990), or it might be the result of the dynamical effects of the X-ray source on the stellar wind (Blondin 1994).

Vela X-1 and 4U 1538-52 have moderate X-ray luminosities which cause minor perturbations of the stellar winds through the effects of X-ray ionization. In their analysis of *Ginga* observations of 4U 1538-52, Clark et al. (1994) matched the data against a Monte Carlo computation of X-ray propagation through a spherically symmetric stellar wind model, taking account of X-ray ionization in 12 atomic species of the normal cosmic abundances. Lewis et al. (1992) interpreted their *Ginga* observations of Vela X-1 in light of a similar Monte Carlo calculation of X-ray propagation, considering only neutral, hydrogenic, and completely ionized states of atoms. In contrast to these moderate X-ray luminosity systems, Day & Stevens (1993) found that the effect of X-ray ionization and heating on the stellar wind of the Cen X-3 system, observed by *EXOSAT*, in its high luminosity state ($\sim 10^{38}$ erg s^{-1}) is a major perturbation and responsible for driving an unsymmetrical thermal wind that supplies the accretion flow needed to generate the high X-ray luminosity. They suggested that this thermal wind is responsible for the exponential portion of the density function which they fit to X-ray eclipse transition observations of Cen X-3.

The eclipsing binary pulsar SMC X-1/Sk 160 is an ideal object for a study of the effects of intense X-ray illumination on the stellar wind of a massive early-type star. Lying at a well determined distance in the Small Magellanic Cloud, its optical and X-ray luminosities are, correspondingly, well determined. Its small optical extinction of $A_V = 0.1$ (van Paradijs & Zuiderwijk 1977) assures that the effects of interstellar absorption and dust grain scattering on the X-ray phenomena are minimal. Its high X-ray brightness and rapid pulsations permit accurate averages of data to be obtained in integration times that

are short compared to the orbital period. And finally, the other sources in the field of view during the *Ginga* observation of SMC X-1 are sufficiently distant, few and soft as to cause no significant contamination of the data.

SMC X-1 was discovered by Leong et al. (1971), its eclipses and orbital period by Schreier et al. (1972), and pulsations by Lucke et al. (1976). The B0I star Sk 160 was suggested to be the optical counterpart by Webster et al. (1972), and confirmed by Liller (1973) who observed the correlation between the ellipsoidal variation of the optical light curve and the X-ray orbital variation. van Paradijs & Zuiderwijk (1977) demonstrated that the variation of the optical phenomena of Sk 160 cannot be explained as ellipsoidal variations alone; they attributed the peculiar variations to the light emitted by an accretion disk in the binary system. A recent precise X-ray timing analysis of SMC X-1 using the present *Ginga* observations has been presented by Levine et al. (1993). Current values of the parameters of the SMC X-1/Sk 160 system are listed in Table 1.

High resolution IUE spectra of Sk 160, reported by Hammerschlag-Hensberge, Kallman, & Howarth (1984), showed substantial variations with orbital phase in the P Cygni profiles of the UV absorption lines. At orbital phase 0.5, when the neutron star was in front of the companion star, the equivalent width of Si IV was reduced by 30% compared to the equivalent width at the center of the X-ray eclipse. They also reported that the terminal velocity of the Sk 160 wind at orbital phase 0.5 was about 100 km s^{-1}, reduced from 250 km s^{-1} at the eclipse phase. They showed that the ionization effect of the scattered X-rays on the wind in the X-ray shadow region could suppress Si IV ions moving faster than 600 km s^{-1}. To explain the difference between the observed 250 km s^{-1} terminal velocity and the predicted 600 km s^{-1} terminal velocity they suggested that the wind structure of Sk 160 is significantly different from that of other stars of similar stellar type due to the ionization effects of the scattered X-rays. They predicted that the terminal velocity of the wind from Sk 160 should be about 50% of the average terminal velocity of galactic stars in the same

stellar class.

The observations and data processing of the *Ginga* data are described in Section 2 of this paper. In Section 3 we display the variation with orbital phase of the equivalent neutral column density of matter along the line of sight. Section 4 compares the observed orbital variations of the X-ray spectrum with predictions derived by a Monte Carlo computation of X-ray propagation through the distribution of matter in the hydrodynamical model of Paper I. Results and conclusions are summarized in Section 5.

2. OBSERVATIONS AND DATA ANALYSIS

The *Ginga* observation of SMC X-1 was made from 1989 July 29 to August 3 with the LAC gas proportional counters on the *Ginga* satellite (Makino et al. 1987, Turner et al. 1989). The observation began at orbital phase 0.92 and lasted for 1.3 orbital cycles with the usual gaps due to earth blockages and trapped particle interference. The LAC counters had a honeycomb collimator $1.1° \times 2.0°$ FWHM field of view, a total effective area of 4000 cm^2. Data were recorded in either the MPC-2 mode as 48-channel pulse height distributions (PHDs) with integration times of 0.0625, 0.5, & 2.0 s, or in the MPC-3 mode as 12-channel pulse height channels; 0.0078, 0.0625, & 0.25 sec time resolution. The intrinsic energy resolution of the LAC detectors was 20% FWHM at 5.9 keV.

The *ROSAT* observation of SMC X-1 was made from 1991 October 7.17 to 8.11 (orbital phase 0.47 to 0.71) with the X-ray telescope and position sensitive proportional counter (PSPC) the combination of which had an angular resolution of ~ 25 arcsec, a 2° (diameter) field of view, and an energy sensitivity in the range from 0.1 to 2.5 keV. The energy resolution of the PSPC was 48% at 0.98 keV.

The *ROSAT* image of the field surrounding SMC X-1 is shown in Figure 1 with the

Ginga field of view superimposed. The several weak sources in the *Ginga* field of view have a total *ROSAT* counting rate less than 1% of the *ROSAT* counting rate of SMC X-1. Since most of these nearby sources have very soft spectra, they were detected with much less efficiency by the *Ginga* LAC than by the *ROSAT* PSPC and therefore made little or negligible contribution to the *Ginga* data.

We corrected the raw PHD of the *Ginga* data for particle-induced background by subtracting an estimate derived from an algorithm (Hayashida et al. 1989) which includes the effects of radioactive decay of activities induced in the detector by trapped charged particles in the South Atlantic Anomaly. We then averaged the PHDs over 128-second integration intervals. Plots of these background-subtracted data in five pulse height ranges are shown in Figure 2 with Poisson statistic error bars. The continuous lines are the calculated light curves derived from the hydrodynamical model as described in Section 4 below.

3. EQUIVALENT NEUTRAL COLUMN DENSITY DISTRIBUTIONS

Our first objective was to display the variation of the column density of matter along the line of sight to the X-ray star. To this end we subtracted from each of the 128-s PHDs the average PHD recorded during the period of deep eclipse to remove the contributions of scattered X-rays from circumsource matter and X-rays from other sources in the field of view. Each of the 128-s PHDs was then fitted by a model PHD computed as a convolution of the LAC response matrix with the following spectrum function expressed as photons cm^{-2} s^{-1} $(keV)^{-1}$ and composed of an absorption factor multiplied by the sum of three component spectra: a Planck function, a power law, and a Gaussian iron emission line (all energies expressed in keV):

$$I(E) = \exp[-\sigma(E)N_H][f_{bb}(E) + f_{pl}(E) + f_{Fe}(E)], \tag{1}$$

where

$$f_{bb}(E) = I_{bb}(E/E_{bb})^2(\epsilon - 1)(\exp[E/E_{bb}] - 1)^{-1},$$

$$f_{pl}(E) = I_{pl}E^{-\alpha} \left\{ \begin{array}{ll} 1, & E < E_c \\ \exp\left[-\frac{E-E_c}{E_f}\right], & E \geq E_c \end{array} \right\},$$

$$f_{Fe}(E) = I_{Fe}(2\pi\sigma_{Fe}^2)^{-1/2}\exp\left[-\frac{(E-E_{Fe})^2}{2\sigma_{Fe}^2}\right].$$

I_{bb} is the black body intensity at $E = E_{bb}$, I_{pl} is the power law intensity at $E = 1$ keV, I_{Fe} is the total iron line intensity, and ϵ is the basis of natural logarithm. The shape parameters are the black body temperature E_{bb}, the power law index α, the "cutoff" and "folding" energies E_c and E_f, and the center energy E_{Fe} and width σ_{Fe} of the iron line. For the purpose of this preliminary survey of the column density we ignored the effects of X-ray ionization on the attenuation cross section and assumed it to be $\sigma(E) = \sigma_{ph}(E) + 1.21\sigma_T$ where $\sigma_{ph}(E)$ is the photoelectric absorption cross section of cold matter given by Morrison & McCammon (1983) and σ_T is the Thompson scattering cross section. We call the fitted value of the parameter N_H the "equivalent neutral column density." We note that an unpulsed black body component with $E_{bb} = 0.16$ keV was detected in the analysis of *Einstein* SSS observations of SMC X-1 by Marshall et al. (1983).

Statistical fluctuations in the 128-s PHDs of the *Ginga* data recorded during the eclipse would have caused large uncertainties in the fitted values of the spectrum parameters if all ten were allowed to vary in each of the fitting processes. Therefore, we fixed the six shape parameters at values determined from a fit to data of high statistical accuracy derived from the MPC-2 mode observations in channels 3 to 45 during the non-eclipse orbital phases between 0.30 and 0.45 when the X-ray attenuation was relatively low. We also fitted a convolution of the *ROSAT* response matrix with the same function (minus the iron line) to the average *ROSAT* PHD. The resulting two sets of fitted values of the spectrum parameters are listed in Table 2, and the observed and fitted PHDs are displayed in Figures 3 and 4. We note that the black body component contributed very little to the *Ginga* data

and is therefore poorly determined in that fit. Its importance in fitting low energy data is confirmed, however, by the role it plays in the *ROSAT* fit.

Figure 5 shows the variation with orbital phase of N_H and the component intensities, the latter displayed as their ratios to the *Ginga* values in Table 2. To reduce the statistical fluctuations of the plot, we averaged the data points over integration periods extending from the end of each data gap (due to earth blockage and trapped particle interference) to the beginning of the next.

Sharp increases of N_H near the orbital phases 0.1, 0.9 and 1.1 in Figure 5 indicate the X-ray eclipse transitions. The same figure shows that the fitted normalization factor I_0 decreases as N_H increases. This trend is caused by our use in this preliminary analysis of X-ray cross sections for neutral matter instead of ionized hot gas. The ratio of the X-ray opacity of the low energy band (< 6 keV) to the high energy band (> 7 keV) of the ionized gas is much less than that of the cold gas. Hence, to compensate for this difference, the cold matter fit decreases the normalization factor and the column density.

More detailed plots of N_H during the eclipse transitions are shown in Figure 6. The two pre-eclipse peaks in panel (b) of the figure may be caused by absorption in a narrow stream of matter from Roche lobe overflow which feeds an accretion disk and comes into the lines of sight near orbital phase 0.9. The presence of such a stream-fed accretion disk is indicated by the steadiness and ultra-high intensity of the X-ray source. In contrast, pure wind-fed X-ray binaries exhibit highly variable and moderate X-ray intensities, e.g. Vela X-1 and 4U 1538-52. Similar absorption features have been observed in other eclipsing X-ray binaries, e.g., *EXOSAT* observations of Her X-1 and LMC X-4 (Dennerl 1991). Absorption features caused by large scale density fluctuations such as the 'photoionization wake' described in Paper I are probably broader. In any case, such narrow features are likely to be highly variable in time, and not part of the general flow pattern. Therefore, the data from this

period were not used in our analysis which is aimed at probing the distribution of matter in the stellar wind.

During the uneclipsed phase of the orbit the value of N_H is at levels about six times greater than the column density of interstellar neutral hydrogen inferred from the low value of optical extinction and 21-cm radio measurements. The small but significant variation between phases 0.6 and 0.7 is evidence that this high column density is due to matter close to the binary system and therefore subject to change as the orbital motion of the neutron star moves the line of sight back and forth over the circumstellar matter distribution.

4. COMPARISON OF OBSERVATIONS AND SIMULATIONS

We compared the X-ray observations described above with a theoretical model for SMC X-1 by using a Monte Carlo technique to propagate X-rays through the circumstellar gas distribution generated in a 3D hydrodynamic simulation. We describe the essential results of the hydrodynamic simulation here, and refer the reader to Paper I for further details of the numerical model.

Viewed in a reference frame rotating with the orbital period of the system, atmospheric matter in the X-ray shadow of the primary is accelerated outward on a spiral course by radiation pressure, gravity, and the Coriolis force. These are the normal conditions for generation of a line-driven stellar wind by a B0 supergiant. However, in the present system, when matter in the wind passes out of the shadow into the X-ray illuminated region, it becomes so highly ionized that the radiation pressure caused by resonant scattering of the primary's UV radiation by slightly ionized metal ions is effectively turned off. The resulting distribution of matter is highly asymmetric with respect to the line of centers of the binary system due to binary rotation. The biggest effect on observed column densities is expected during eclipse egress, where the radiatively driven wind is deflected out of

the X-ray shadow by the Coriolis force. On the eclipse ingress side of the system, the Coriolis force deflects the stalled radiatively driven wind back into the X-ray shadow, with relatively little effect on the line of sight column density. On the X-ray illuminated side of the primary, X-ray heating drives matter off the stellar surface in the form of an intense thermal pressure-driven wind. In the model of Paper I the mass loss rate in this thermal wind is $\dot{M} \approx 5 \times 10^{-6} M_\odot$ yr^{-1}. In the case of the thermally driven wind, the action of the Coriolis force and the thermal pressure gradients again lead to an asymmetric distribution of wind material. In this case the biggest effect on observed column densities is expected during eclipse ingress. Though the effects of the neutron star gravity on the flow of the thermal wind are neglected in the model, one can assume that the neutron star captures some of the wind and generates an accretion wake with density enhancements that may be perceived in the variation of the column densities measured during the uneclipsed portions of the orbit cycle.

Shown in Figure 7a are three different inclination-angle slices ($i_c = 90°, 70°, 60°$) of density contour maps generated by the 3D hydrodynamic simulation (see paper I) at three different dynamical evolution times ($t = 7.4$ d, 7.8 d). Figure 7b shows plots of the column densities of hydrogen atoms against orbital phase for the density distribution at $t = 7.4$ & 7.8 d the inclination angles $i_c = 60°$ & $70°$.

We used the Monte Carlo code previously employed by Clark et al. (1994) in a study of 4U 1538-52 to compute the spectrum of X-rays emitted in various directions from the system after propagation through the circumstellar matter distributions. The output of the Monte Carlo code is a propagation transfer matrix which specifies the probability that an X-ray photon of a given energy emitted by the source in a random direction distributed isotropically will give rise to a photon with energy in a specified narrow range and direction in a specified element of solid angle. By convolving the transfer matrix with a source spectrum we predict the spectrum of X-rays emitted by the system in any given direction.

The emerging spectrum is further modified by absorption in cold interstellar matter. From these results we derive the predicted spectrum that would be observed at any given orbital phase for a given inclination of the orbital plane. Finally, we convolve the detector response matrix with the in-coming spectra to generate the predicted PHDs.

The code launches X-ray photons of a specific energy from the neutron star in directions uniformly distributed among $\sim 4 \times 10^4$ equal $1° \times 1°$ elements of solid angle over the entire sphere. Each photon is tracked in steps of up to one-tenth of a mean interaction length. At each step a photon may be Compton scattered into a different direction with an energy reduced by the Compton shift, or photoelectrically absorbed with the possible emission of a fluorescent X-ray photon. The photoelectric absorption cross section of the photon at a specific location is determined from the photoelectric absorption cross section table (Figure 8) according to the local ionization parameter. Before running the Monte Carlo computation, we calculated the local ionization parameter over the entire circumstellar region by propagating the source spectrum through the stellar atmospheric density model and tabulating the results in a 2-dimensional table of $\sim 4 \times 10^4$ solid-angle intervals by 83 radial intervals with the width of the radial intervals increasing with distance from the center.

Exit directions and energies of the escaping photons are tabulated in an array corresponding to the same $\sim 4 \times 10^4$ elements of solid angle into which the photons are launched. The resulting tabulations are used to construct the desired transfer matrix, which maps a given source spectrum of isotropically emitted X-ray from the neutron star into the propagated spectrum at a distant point in any given direction. In a complete run, 500 photons at each of 40 energies from 0 to 70 keV in each of the $\sim 4 \times 10^4$ directions are launched. We ran the Monte Carlo computations to generate propagation transfer matrices of X-ray propagation through the circumstellar matter distributions generated in the 3D hydrodynamic simulation at two different times from the start of the simulation.

Backward scattering from the companion star, giving rise to X-ray albedo, is dominately multiple scattering. Since the probability of photoelectric absorption decreases with energy, the chances of a photon scattering backward before it is absorbed increases with energy. Thus the contribution of X-ray albedo to the transfer efficiency in directions from which the neutron star appears in front of the primary increases with energy and can boost the transfer efficiency above unity, as shown in Figure 9. That figure also shows the prominent Fe fluorescent emission line produced by photoelectric absorption above the K edge at 7.1 keV; most of the energy of photoelectrically absorbed X-rays below the iron K edge is lost in other physical processes not included in the Monte Carlo code (such as the Auger process and dielectronic recombination).

Since the spectrum of albedo X-rays differs from that of the source, it is necessary to take the albedo into account in deriving a proper estimate of the intrinsic source spectrum from the average low absorption PHD recorded during the orbit phase interval from 0.30 to 0.45. We therefore re-determined the source spectrum by fitting the low-absorption average PHD with a calculated PHD computed as a convolution of the LAC response matrix with a spectrum derived by convolving the propagation transfer matrix with the spectral function of Equation 1 and multiplying the result by an absorption term representing the interstellar absorption in cold matter with $N_H = 5 \times 10^{20}$ H atoms cm^{-2}. Since the circumstellar absorption is accounted for in the propagation transfer matrix, N_H was set to zero in the source function. The fitted result is summarized in Table 3.

In Figure 2 the calculated light curves for the density distribution model of $t = 7.8$ d of the computational evolutionary time are plotted on top of the data representing the observed counting rates in five energy bands. In Figure 10 to 12 the calculated PHDs for ingress and egress are plotted on top of the observed 384-s averaged PHDs for the observed two egress and one ingress. The calculated PHDs for the eclipse phase are compared with the observed average PHDs in two eclipses in Figure 13.

5. DISCUSSION

5.1. Shadow Wind

Figures 2 and 6 show large differences between the light curves and the column densities observed during the first and second egresses, the second one being much more extended, variable and unsymmetric about the eclipse center relative to the preceding ingress. A qualitatively similar extended, variable and unsymmetric egress is implied by the model, as indicated by the wiggly solid lines of Figure 2 after orbital phase 1.1. The wiggles produced in the 3D model are caused by variations in the column density through the stalled radiatively driven wind coming out of the X-ray shadow: the shadow wind. The variations in column density arise both from the inherent variability of the radiatively driven wind, and from the turbulence generated as some of the stalled shadow wind crashes back to the surface of the primary star. We interpret this qualitative match between the observed and calculated light curves as evidence for the validity of the hydrodynamical simulation and the reality of the shadow wind phenomenon.

5.2. Thermal Wind

In the model, X-ray illumination of the primary's atmosphere on the side facing SMC X-1. while destroying the radiation-driving mechanism of the stellar wind, heats the atmosphere. giving rise to an intense thermal pressure-driven wind with a mass loss rate of $\dot{M} \approx 5 \times 10^{-6} M_{\odot}$ yr^{-1}. Our Monte Carlo calculation shows that the distribution of matter attributable to this thermal wind provides explanations for the following broad features of our observations:

1. The spectrum and intensity of X-rays observed in deep eclipse. That spectrum has the same shape as the spectrum of direct X-rays from SMC X-1 as expected for X-rays that have been Compton-scattered into the eclipse shadow by any circumsource matter. However, the value of the deep eclipse intensity is too large to be explained as a result of scattering from the perturbed wind that was initiated on the shadowed side by the line driving mechanism. The presence of a strong thermally driven wind increases the number of scatterers in the vicinity of the X-ray source and brings the calculated deep eclipse intensity into agreement with the observed intensity.

2. The gradualness of the change in the X-ray spectrum and intensity during eclipse ingress. Without the thermal wind the model would have predicted a sharp ingress because X-ray ionization above the X-ray terminator would prevent formation of an extended atmosphere in the form of a line-driven wind. In our Monte Carlo calculation the gradualness implied by the model is caused by absorption in the enhanced density associated with the thermal wind which is not fully ionized.

3. The high level of the equivalent neutral column density during the uneclipsed portion of the orbit (Fig. 5). As mentioned previously, this level is approximately six times the column density of interstellar matter estimated from optical extinction and 21-cm radio data. Its small but significant variation indicates that the matter responsible for it lies close to the system, i.e., not in a distant and steady cloud. Absorption in the thermal wind and shadow wind beyond the orbit of the neutron star accounts for most of the equivalent column density plotted in Fig. 5.

The small but significant variation in column density between orbital phases 0.2 and 0.8, and especially between 0.6 and 0.7, may have occurred when the line of sight passed through density perturbations associated with an accretion wake and/or tidal stream caused by gravitational deflection of the thermal wind by the neutron star. Such effects were not included in the 3D simulations of Paper I and are therefore absent from our Monte Carlo estimates of the X-ray phenomena.

6. SUMMARY

We have explored the circumstellar environment of the X-ray binary pulsar SMC X-1/Sk 160 by analysis of the X-ray phenomena recorded by *Ginga* LAC during an observation extending over 1.3 orbital cycles including one eclipse ingress and two egresses and by *ROSAT* PSPC during an observation covering the binary orbital phase 0.47 to 0.71. The results are compared with those expected on the basis of a Monte Carlo computation of X-ray propagation through the distribution of circumstellar matter computed numerically in a 3D hydrodynamical model by Blondin & Woo (1994). We find the X-ray phenomena implied by the model to be in general agreement with the observations, thereby lending support to the following interpretation of the observations:

1. The observed asymmetry of the X-ray light curves with respect to the eclipse center (orbit phase 0.0), and the variability of the egress curves reflect the asymmetric distribution of a radiatively driven wind formed in the X-ray shadow. According to the model, a radiatively driven wind develops from the shadowed side of the primary star. As this wind exits from the X-ray shadow the intense X-ray flux destroys the ions essential to the line-driving mechanism, and the wind stalls out. Viewed in a frame rotating with the orbital period, the Coriolis force bends the stalled wind around in a configuration that is asymmetric with

respect to the line joining the centers of the two stars: The stalled shadow wind is bent out of the X-ray shadow (and into the line of sight) on the egress side, and back into the X-ray shadow on the ingress side of the primary star.

2. Compton scattering from the thermal wind accounts for most of the X-rays observed in the deep eclipse.

3. Absorption along the lines of sight through an intense thermal wind ($\dot{M} \approx 5 \times 10^{-6} M_\odot$ yr^{-1}), driven by X-ray heating on the side of the primary facing the neutron star, is the likely cause of the gradualness of the extended eclipse ingress and the initial phase of the egresses.

4. Absorption in the thermal wind and shadow wind beyond the orbit of the neutron star accounts for the high value of the column density (3×10^{21} H atoms cm^{-2}) observed during the uneclipsed portion of the orbit. Additional absorption in density enhancements associated with an accretion wake of the neutron star in the thermal wind is the likely cause of the variability of that column density.

P_{orb}	3.89211564 d	a
$a_X \sin i$	53.4876 lt-s	a
i_c (inclination angle)	$56° - 62°$	d
M_{opt}/M_X	15.8	d
θ_e (eclipse half-angle)	$17° - 25°$	d
R_o (primary radius)	$17.2\ R_\odot$	d
p_{pulse}	0.70981 s	a
L_X^1 (13.6 eV - 13.6 keV)	2.9×10^{38} ergs s^{-1}	e
L_X^2 (0.1 - 3.0 keV)	8.6×10^{37} ergs s^{-1}	e
L_{opt}	5×10^{38} ergs s^{-1}	b
S_P	B0I	b
A_V	0.26 mag	c
distance	50 kpc	f

Table 1: Parameters of the binary system SMC X-1/Sk 160. i_c, θ_e, and R_o are conservative limits. L_X^1 is the source luminosity of the power law component; L_X^2 is the luminosity of the blackbody component only.

[a]Levine et al. 1992

[b]Hutchings et al. 1977

[c]van der Klis et al. 1982

[d]Woo 1993

[e]This work

[f]Adopted

Parameter	ROSAT Value (1σ)	Ginga Value (1σ)
$N_H(10^{22}$ cm$^{-2})$	0.29 (0.03)	0.63 (0.32)
I_{pl} (photons/keV/cm^2/s)	0.044 (0.0087)	0.049 (0.007)
α	0.65 (0.27)	0.93 (0.08)
E_c (keV)		5.64 (0.50)
E_f (keV)		15.03 (1.19)
E_{Fe} (keV)		6.70 (0.26)
σ_{Fe} (keV)		0.77 (0.32)
I_{Fe} (photons/cm^2/s)		0.00079 (0.00040)
E_{bb} (keV)	0.16 (0.01)	0.15 (0.02)
I_{bb} (photons/keV/cm^2/s)	0.633 (0.094)	3.54 (2.40)
χ^2_ν	1.29	1.49

Table 2: Fitted values of the spectral function parameters of the *ROSAT* and *Ginga* PHDs for SMC X-1.

Parameter	Value (1σ)
I_0 (photons/keV/cm^2/s)	0.035 (0.0014)
α	0.75 (0.03)
E_c (keV)	5.15 (0.29)
E_f (keV)	11.14 (0.31)
E_{Fe} (keV)	6.91 (0.22)
σ_{Fe} (keV)	0.0 (fixed)
I_{Fe} (photons/cm^2/s)	0.00031 (0.00013)
χ^2_ν	0.61

Table 3: Parameters of the intrinsic source spectrum of SMC X-1 which yields the observed spectrum at orbit phase $\sim$ 0.5 when propagated through the model matter distribution (including albedo) by the Monte Carlo calculation. A constant neutral gas absorption of $N_H = 5 \times 10^{20}$ H-atoms cm^{-2} is convolved to the transfer matrix.

REFERENCES

Blondin, J. M. 1994, ApJ435, in press

Blondin, J. M. & Woo, J. W. 1994, ApJsubmitted (Paper I)

Castor, J. I., Abbott, D. C., & Klein, R. I. 1975, ApJ, 195, 157

Clark, G. W., Minato, J. R., & Mi, G. 1988, ApJ, 324, 974

Clark, G. W., Woo, J. W., & Nagase, F. 1994, ApJ, 422, 336

Day, C. S. R., & Stevens, I. R. 1993, ApJ, 403, 322

Dennerl, K. 1991, Ph. D. Thesis, Max-Planck-Institut Für Extraterrestrische Physik

Haberl, F., White, N. E., & Kallman, T. R. 1989, ApJ, 343, 409

Hayashida, K., et al. 1989, PASJ, 41, 373

Hammerschlag-Hensberge, G., Kallman, T. R., & Howarth, I. D. 1984, ApJ, 283, 249

Heap, S. R., & Corcoran, M. F. 1992, ApJ, 387, 340

Hutchings, J. B., Crampton, D., Cowley, A. P., & Osmer, P. S. 1977, ApJ, 217, 186

Kallman, T. R., & Krolik, J. H. 1994, XSTAR, A Spectral Analysis Tool

Leong, C., Kellog, E., Gursky, H., Tananbaum, H., & Giacconi, R. 1971, ApJ, 170, L67

Levine, A., Rappaport, S., Deeter, J. E., Boynton, P. E., & Nagase, F. 1993, ApJ, 410, 328

Lewis, W., Rapparport, S., Levine, A., & Nagase, F. 1992, ApJ, 389, 665

Liller, W. 1973, ApJ, 184, L37

Lucke R., Yentis, D., Freidman, H.. Fritz, G., & Shulman, S. 1976, ApJ, 206. 625

Makino, F., & the ASTRO-C team, 1987, Ap. Lett. comm., 25, 223

Marshall. F. E., White, N. E., & Becker, R. H. 1983, ApJ. 266, 814

Morrison, R., & McCammon D. 1983. ApJ, 270. 119

Poe, C. H.. Owocki, S. P.. & Castor, J. L. 1990, ApJ, 358, 199

Sato. N. et al. 1986. PASJ. 38. 731

Schreier. E.. Giacconi. R.. Gursky. H.. Kelley. E.. & Tananbaum, H. 1972, ApJ, 178, L71

Schreier. E. J.. Swartz. K., Giacconi. R.. Fabbiano, G., & Morin, J. 1976, ApJ204. 539

Turner, M.. et al. 1989. PASJ, 41, 345

van der Klis, M., Hammerschlag-Hensberge, G., Bonnet-Bidaud, J. M., Ilovaisky, S. A., Mouchet, M., Glencross, W. M., Willis, A. J., van Paradijs, J. A., Zuiderwijk, E. J., & Chevalier, C. 1982, A&A, 106, 339

van Paradijs, J., & Zuiderwijk, E. 1977, A&A, 61, L19

Webster, B. L., Martin, W. L., Feast, M. W., & Andrews, P. J. 1972, Nature Phys. Sci., 240, 183

Woo. J. W. 1993. Ph. D. Thesis, MIT
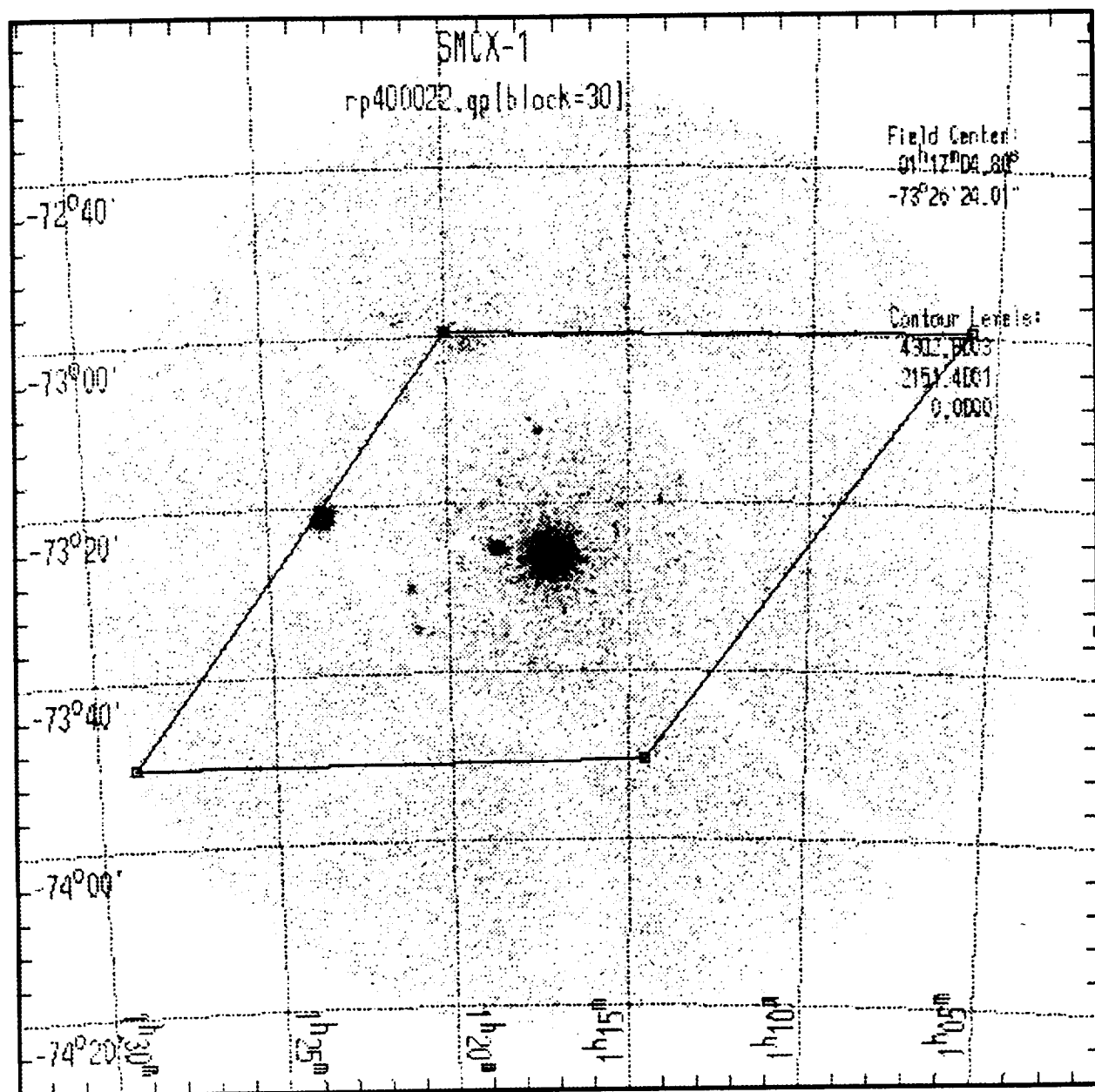
Fig. 1.— *ROSAT* image of SMC X-1. The superposed solid-line diamond represents the *Ginga* FWHM field of view at the time of *Ginga* SMC X-1 observation.
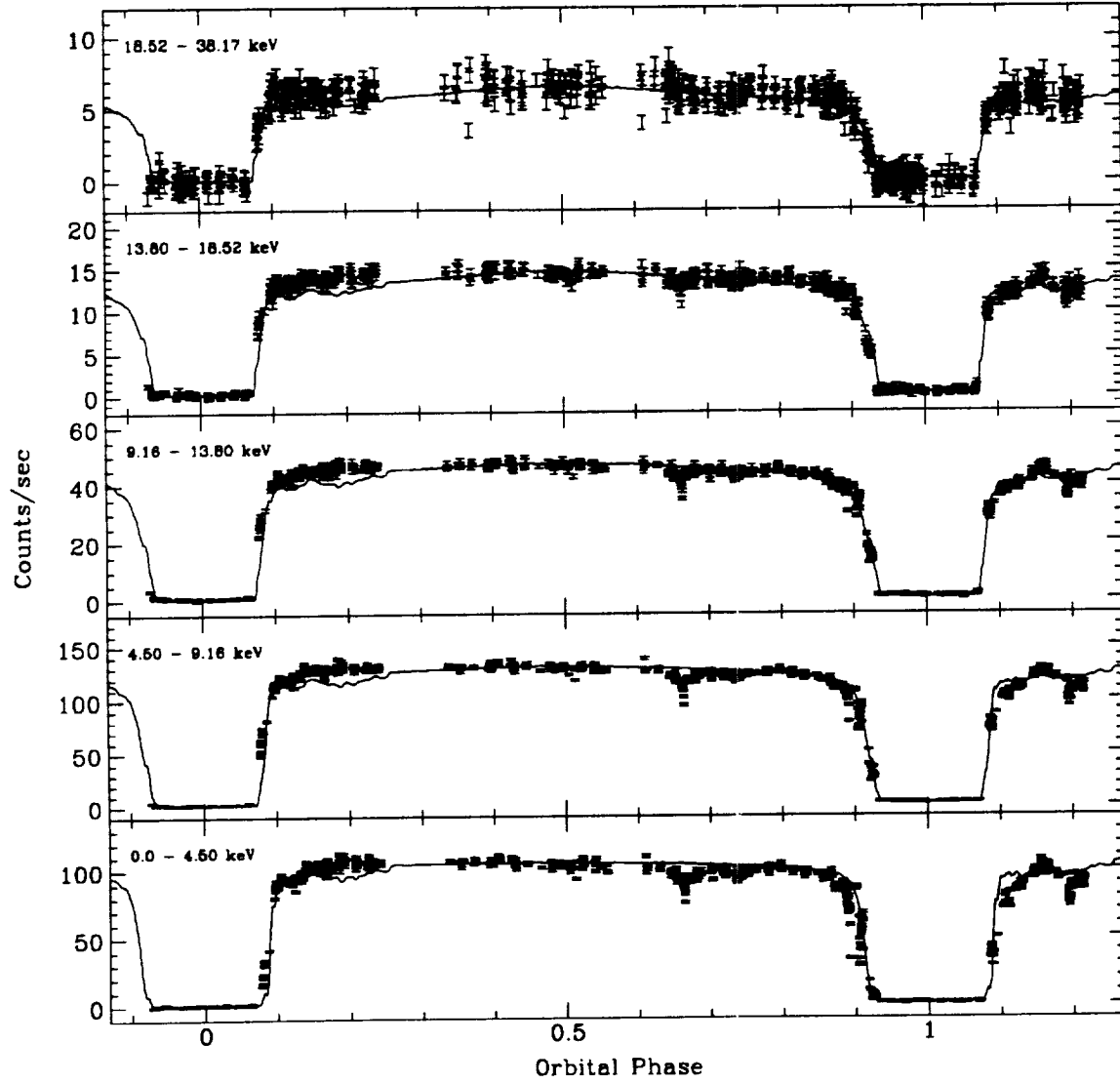
Fig. 2.— Observed counting rates in five energy bands (data points with statistical error bars), and calculated X-ray light curves derived from the distribution of circumstellar matter in the 3D hydrodynamical model of Paper I.
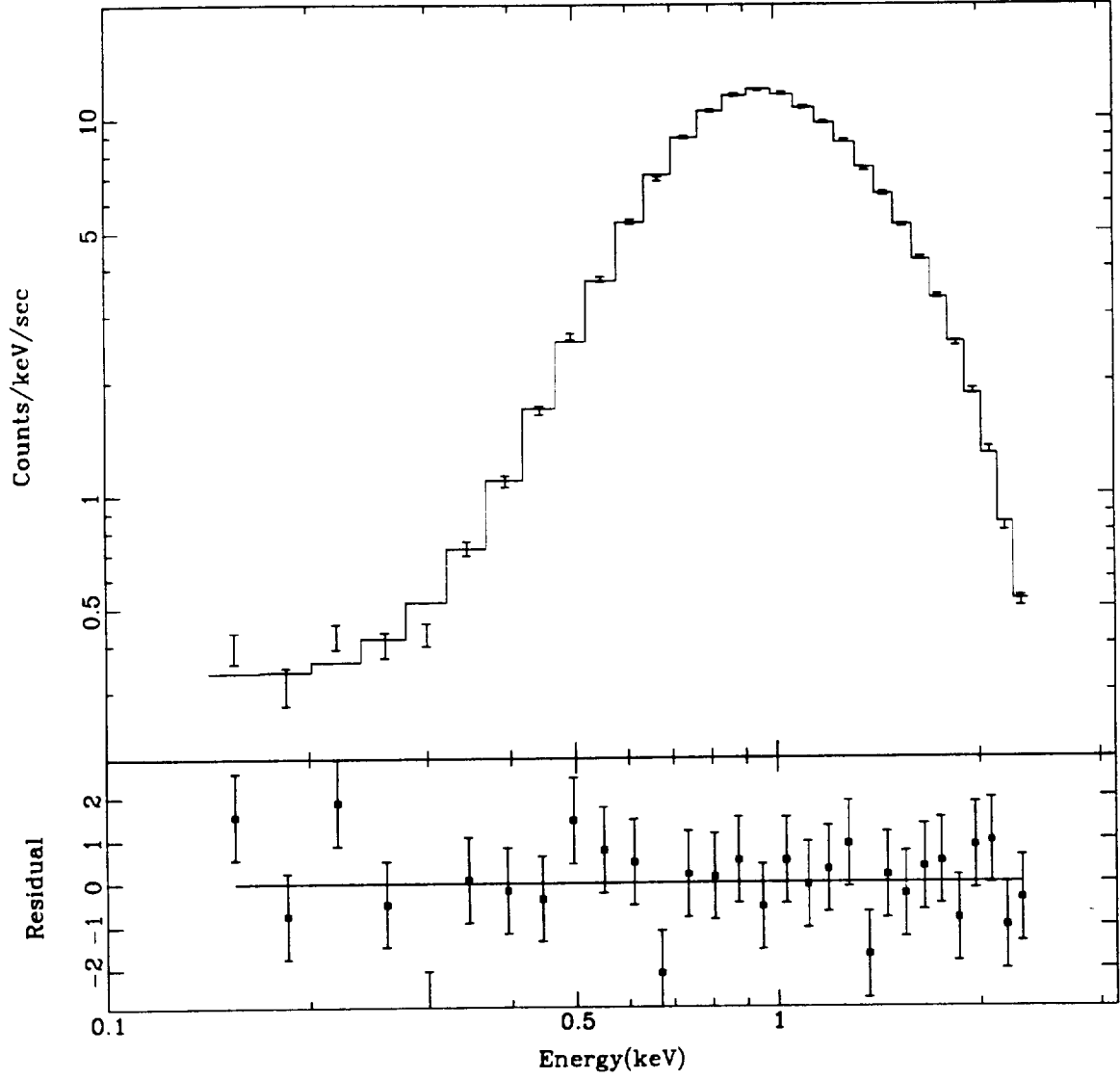
Fig. 3.— *ROSAT* average PSPC PHD of X-rays recorded during the orbital phase interval from 0.47 to 0.73. The histogram is the fitted distribution. The residuals of observed and fitted PHDs are shown in the lower panel.
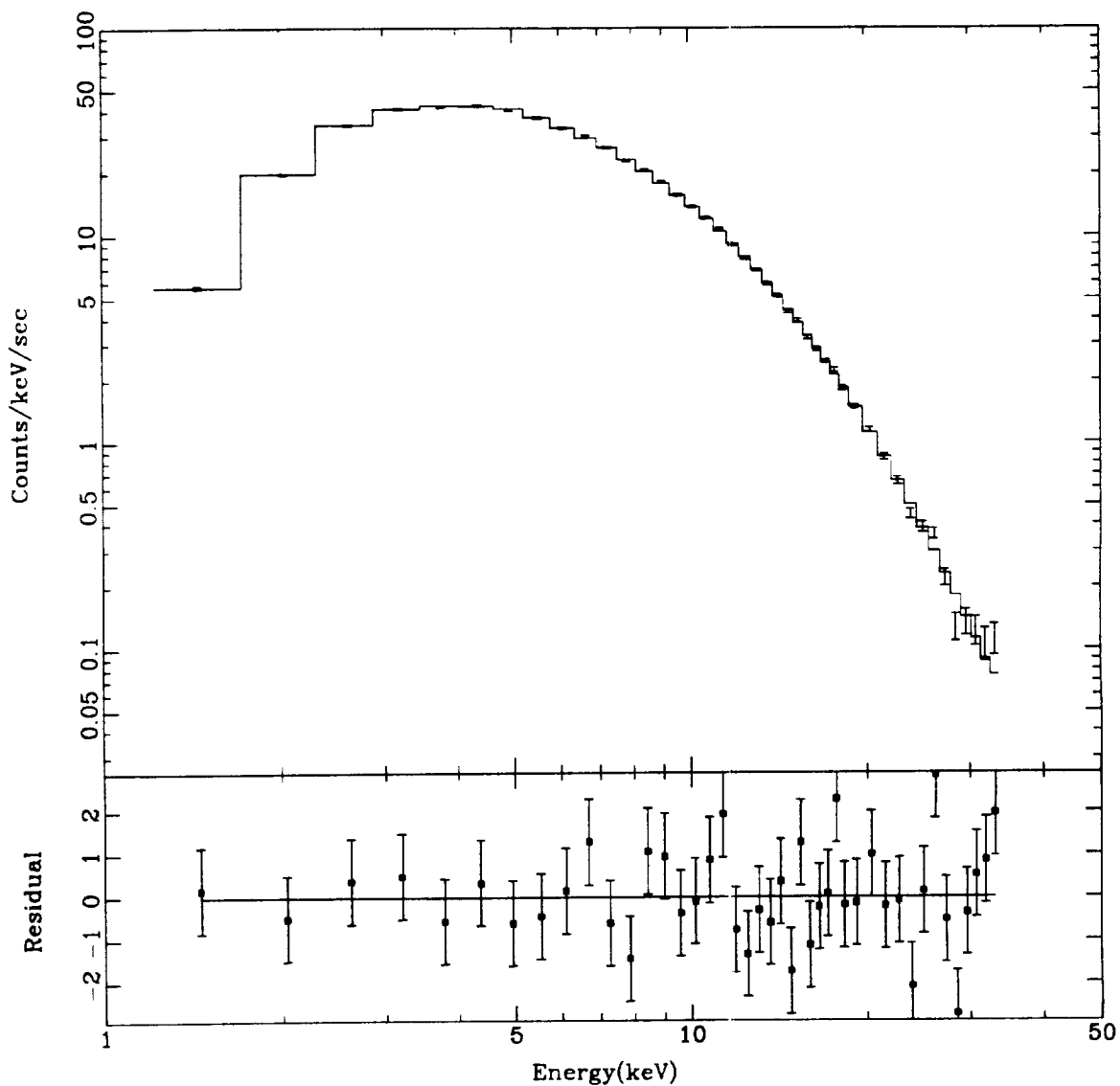
Fig. 4.— *Ginga* average PHD of X-rays recorded during the orbital phase interval from 0.3 to 0.45. The solid-line histogram is the fitted distribution. The residuals of observed and fitted PHDs are shown in the lower panel.
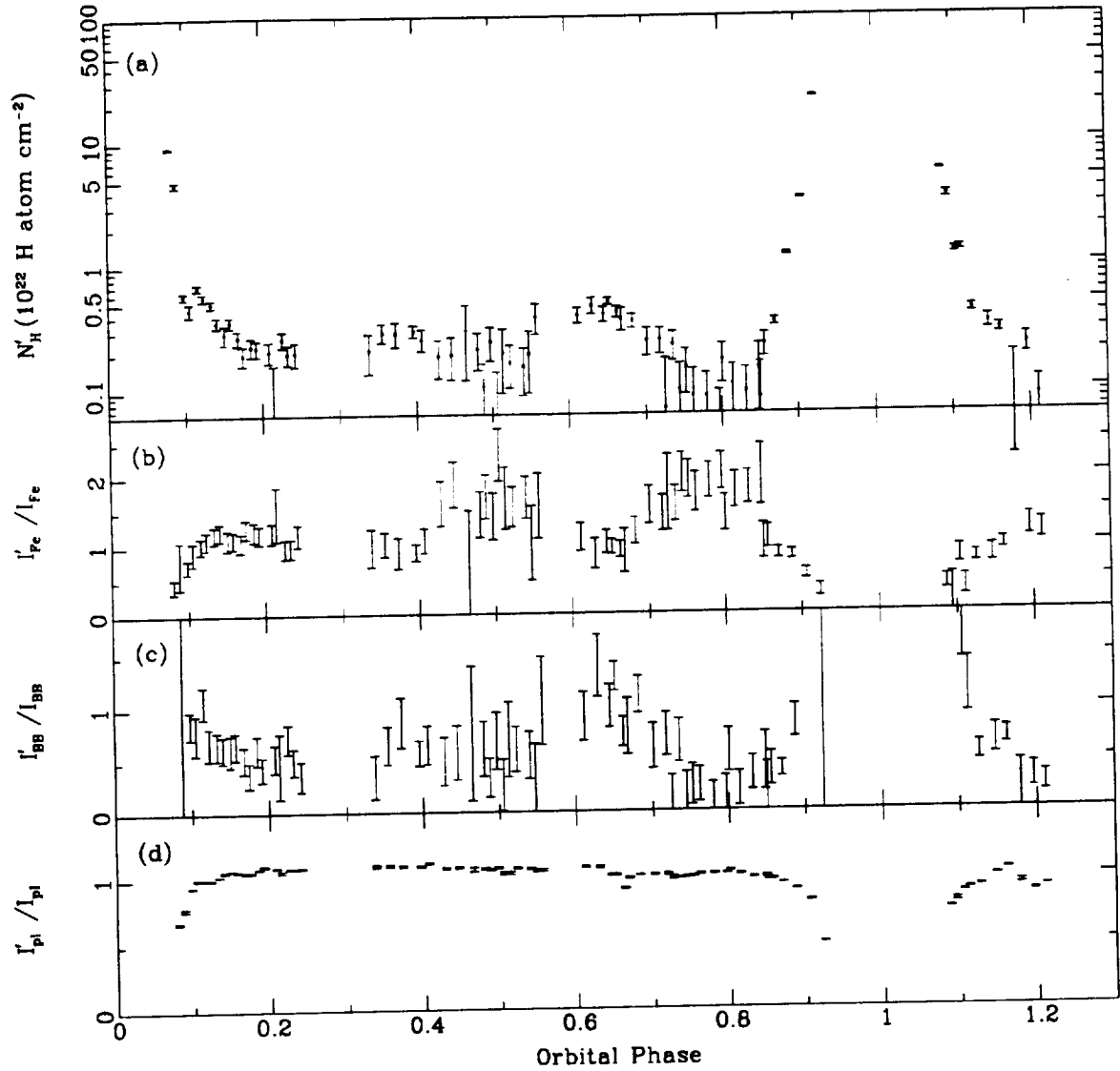
Fig. 5.— Plots of fitted values against orbital phase: (a) column density of hydrogen atoms:
(b) iron intensity variation, (c) normalization variation of the black body component, and
(d) normalization variation of the power law component relative to the fitted values of Table
2. Each data point represent an average fitted value between two successive data gaps.
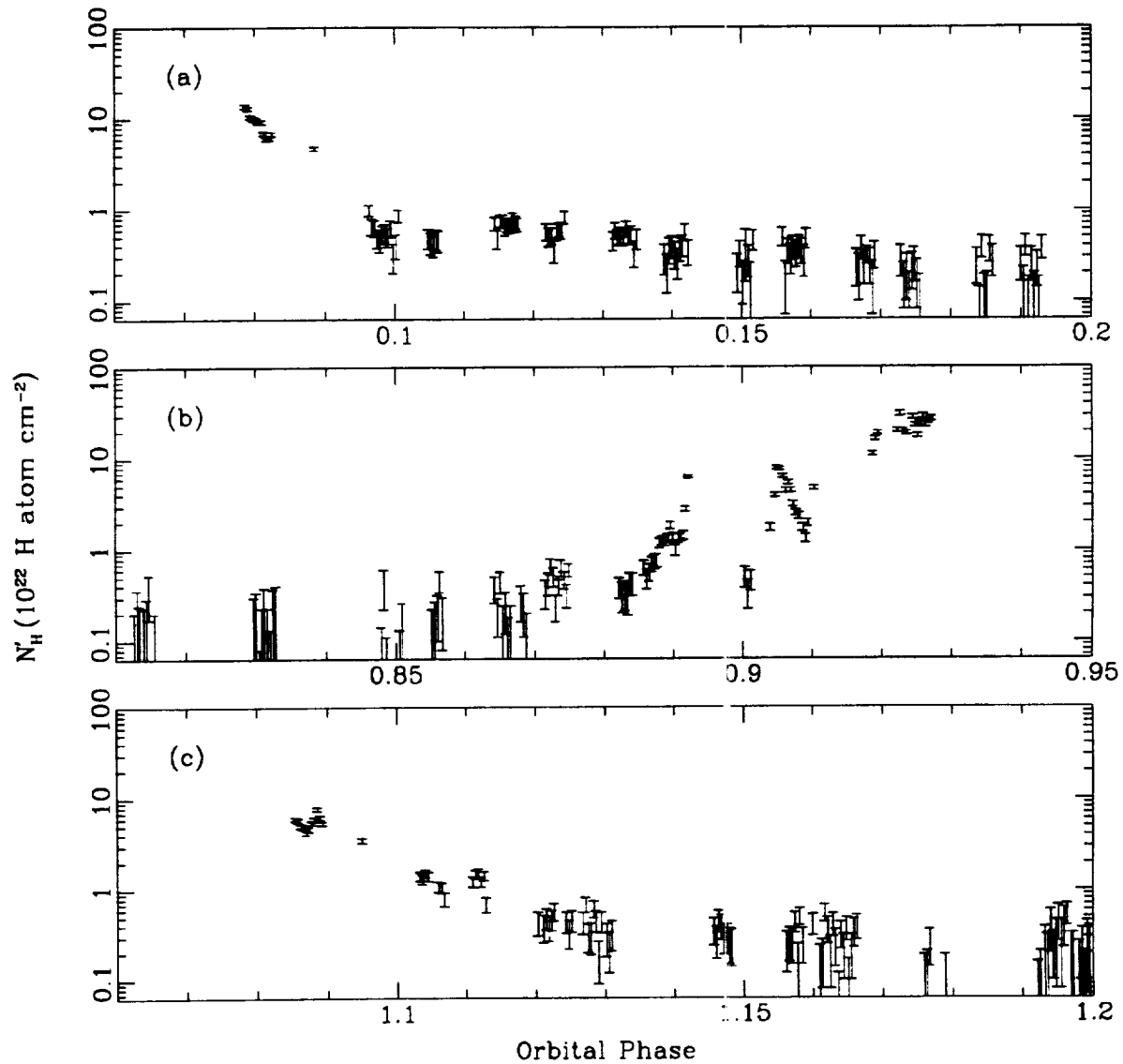
Fig. 6.— Column densities derived from the spectrum fits during (a) the egress transition of the first eclipse, (b) the ingress transition of the second eclipse, and (c) the egress transition of the second eclipse. Each data point represents a 128-s averaged PHD.
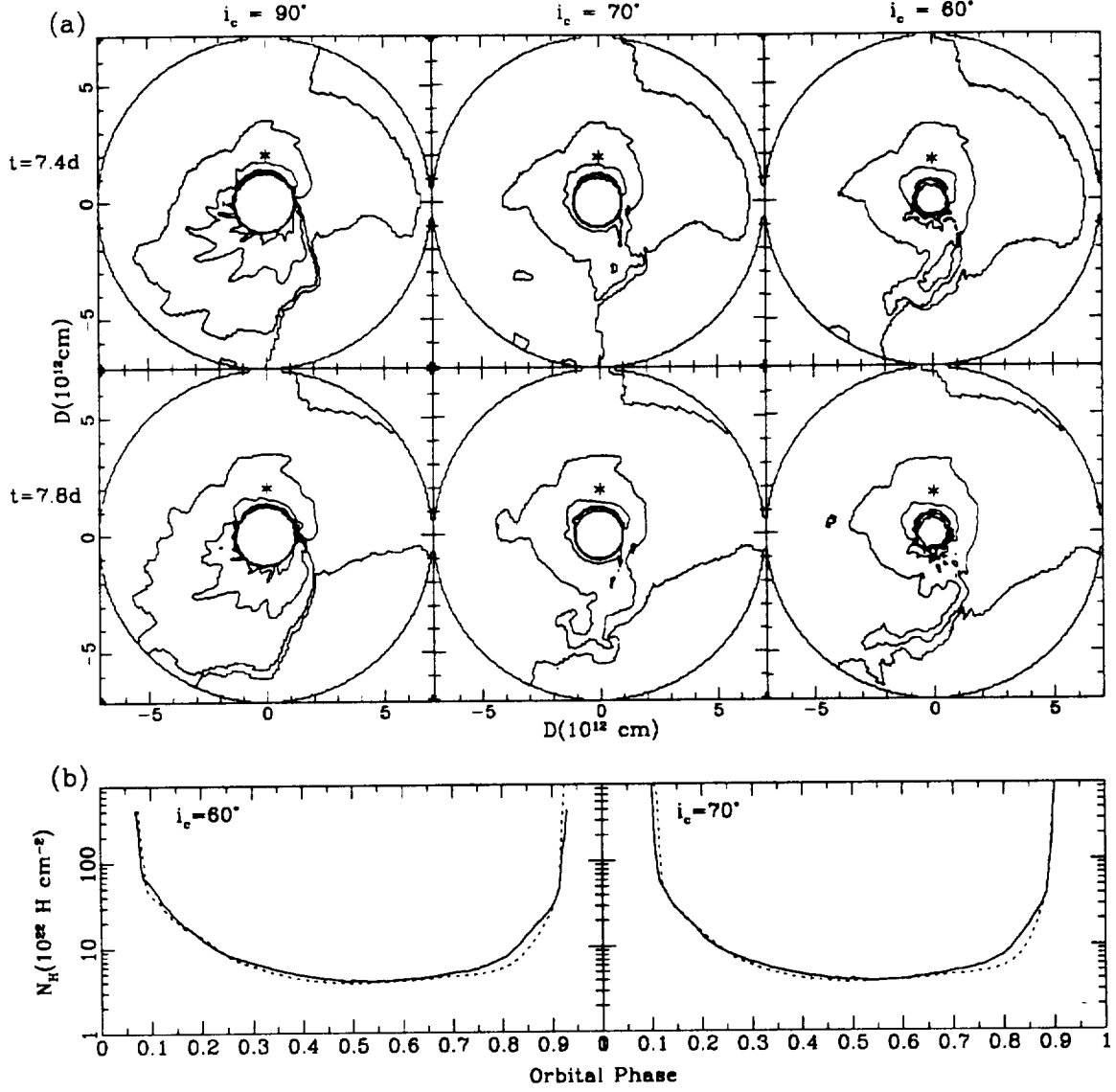
Fig. 7.— (a) Contour density maps of the SMC X-1 system from hydrodynamic simulations at evolutionary times: $t = 7.4$ & 7.8 d. The three columns represent slices from the 3D model with 90°, 70°, and 60° inclination angles about the neutron star. (b) Column densities plotted against X-ray orbital phase calculated from the 70° & 60° inclination angle planes of two 3D hydrodynamic simulations at $t = 7.4$ d (solid-lines) & 7.8 d (dotted-lines).
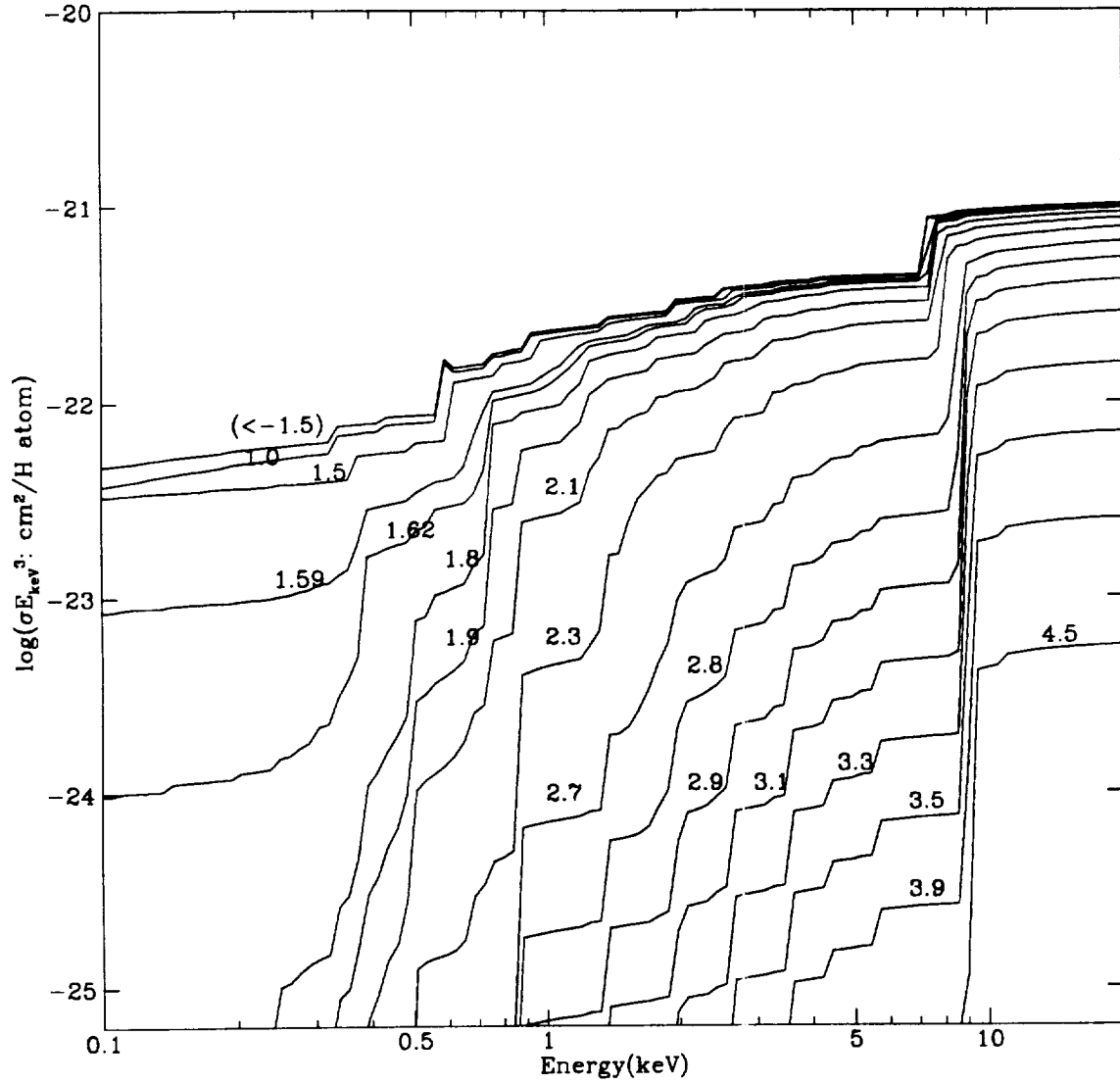
Fig. 8.— Photoelectric absorption cross sections computed by the XSTAR code (Kallman & Krolik 1994) for the various values of the ionization parameter $\log \xi$.
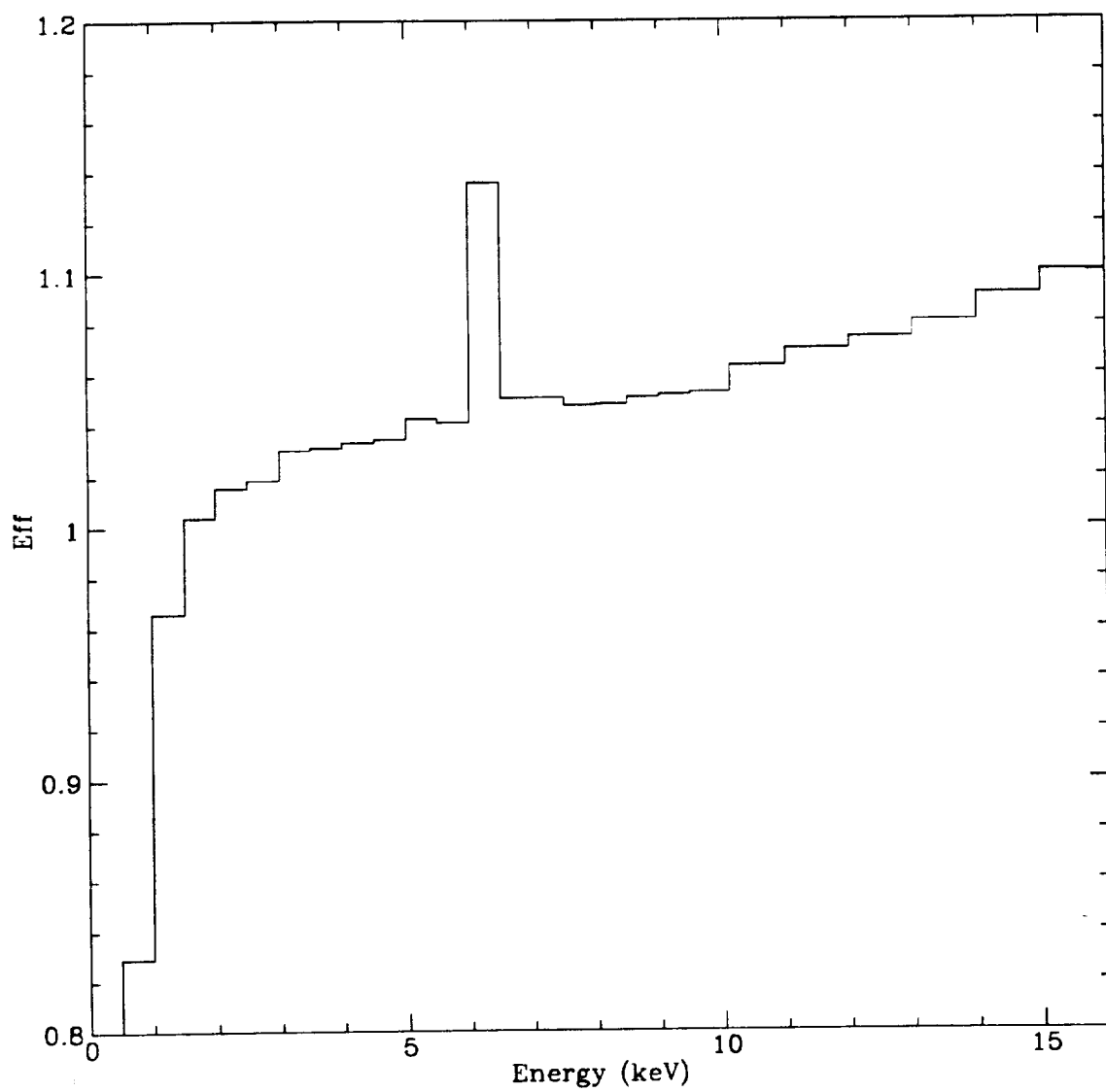
Fig. 9.— Average albedo transfer efficiency for the SMC X-1 spectrum around 0.5 orbital phase plotted against the photon energy.
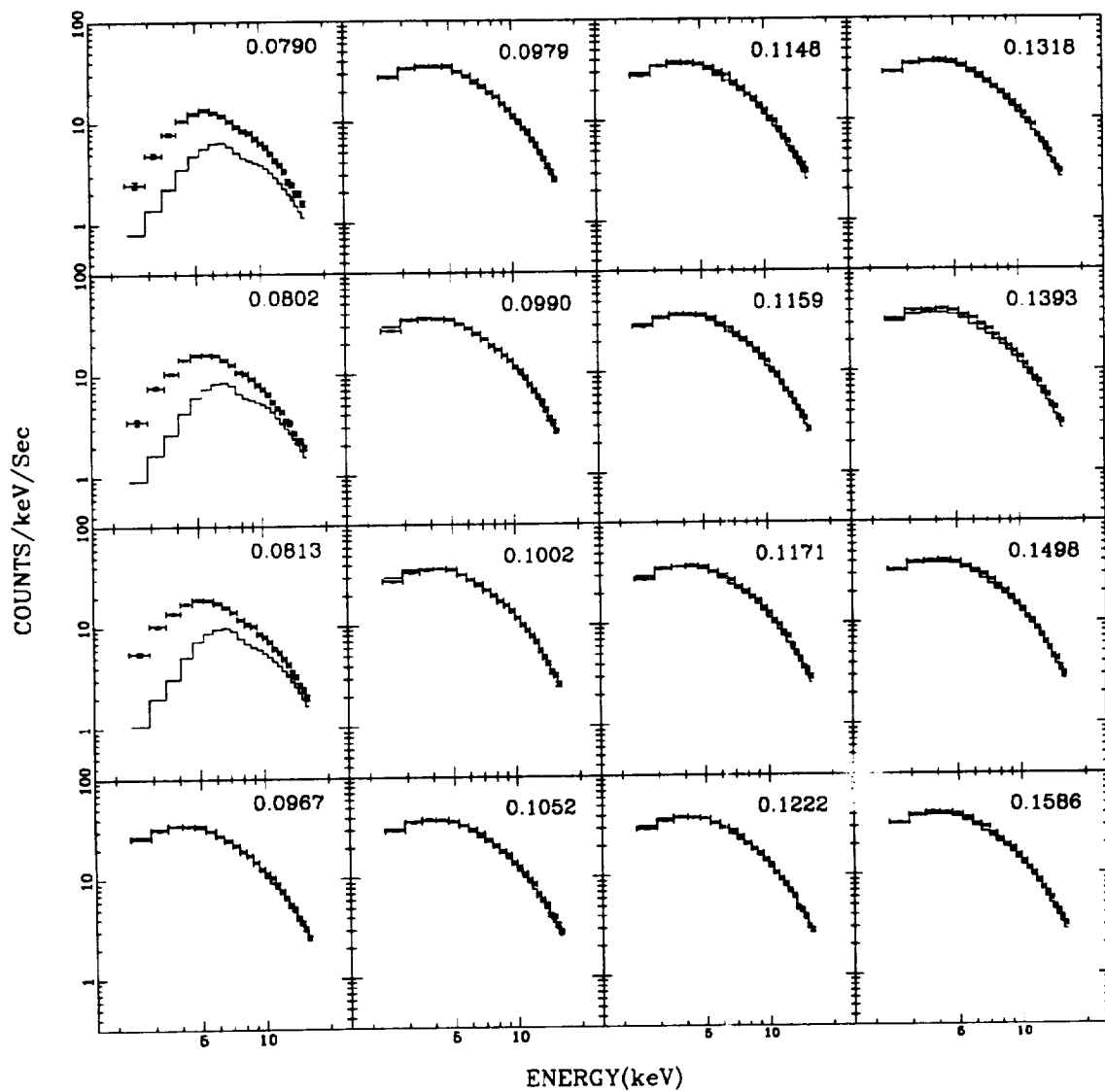
Fig. 10.— PHDs computed by the Monte Carlo method for the first eclipse egress transition. The orbital phase of each PHD is indicated on the upper right-hand corner.
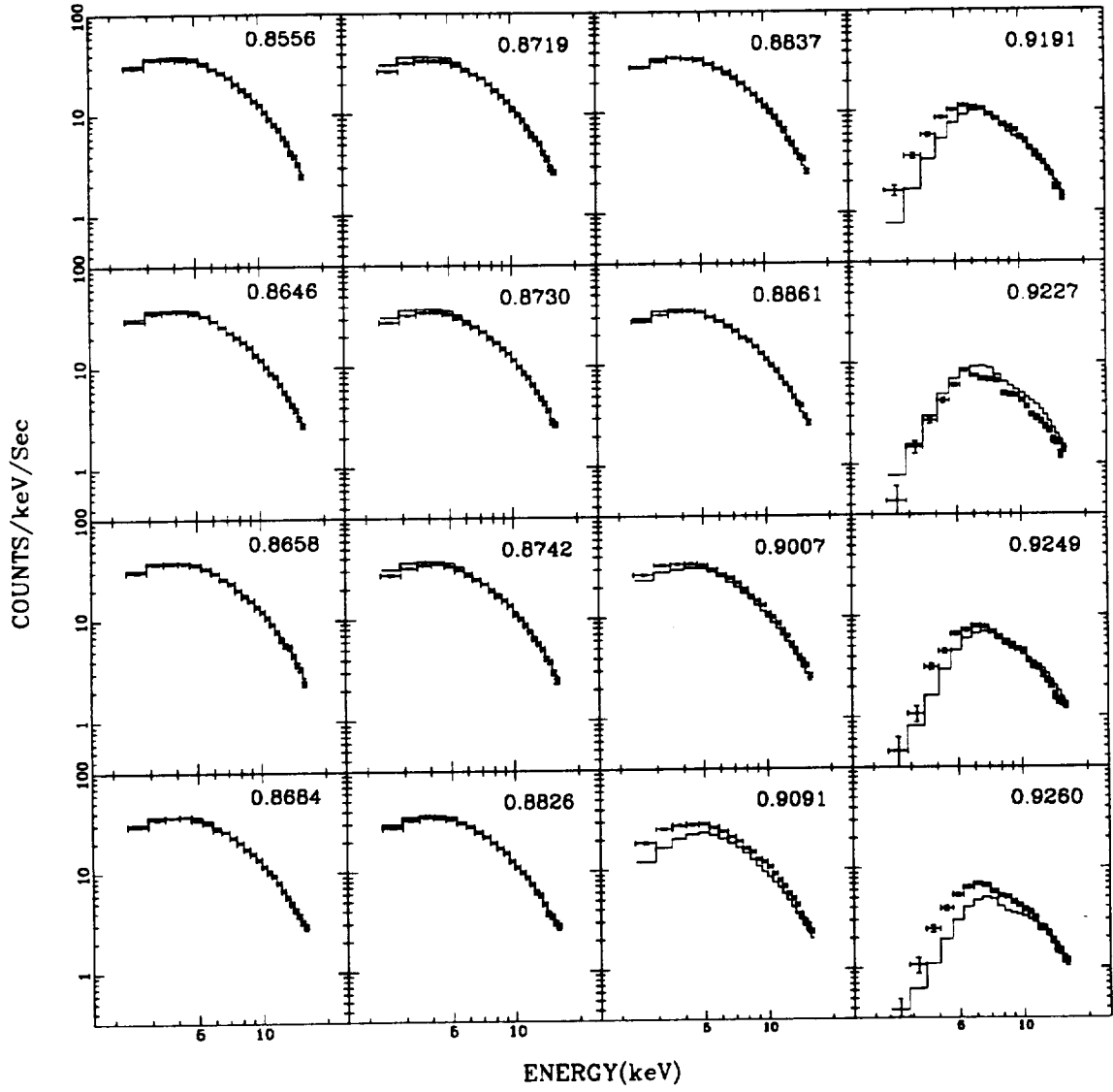
Fig. 11.— Computed PHDs for the second eclipse ingress transition. The orbital phase of each PHD is indicated on the upper right-hand corner.
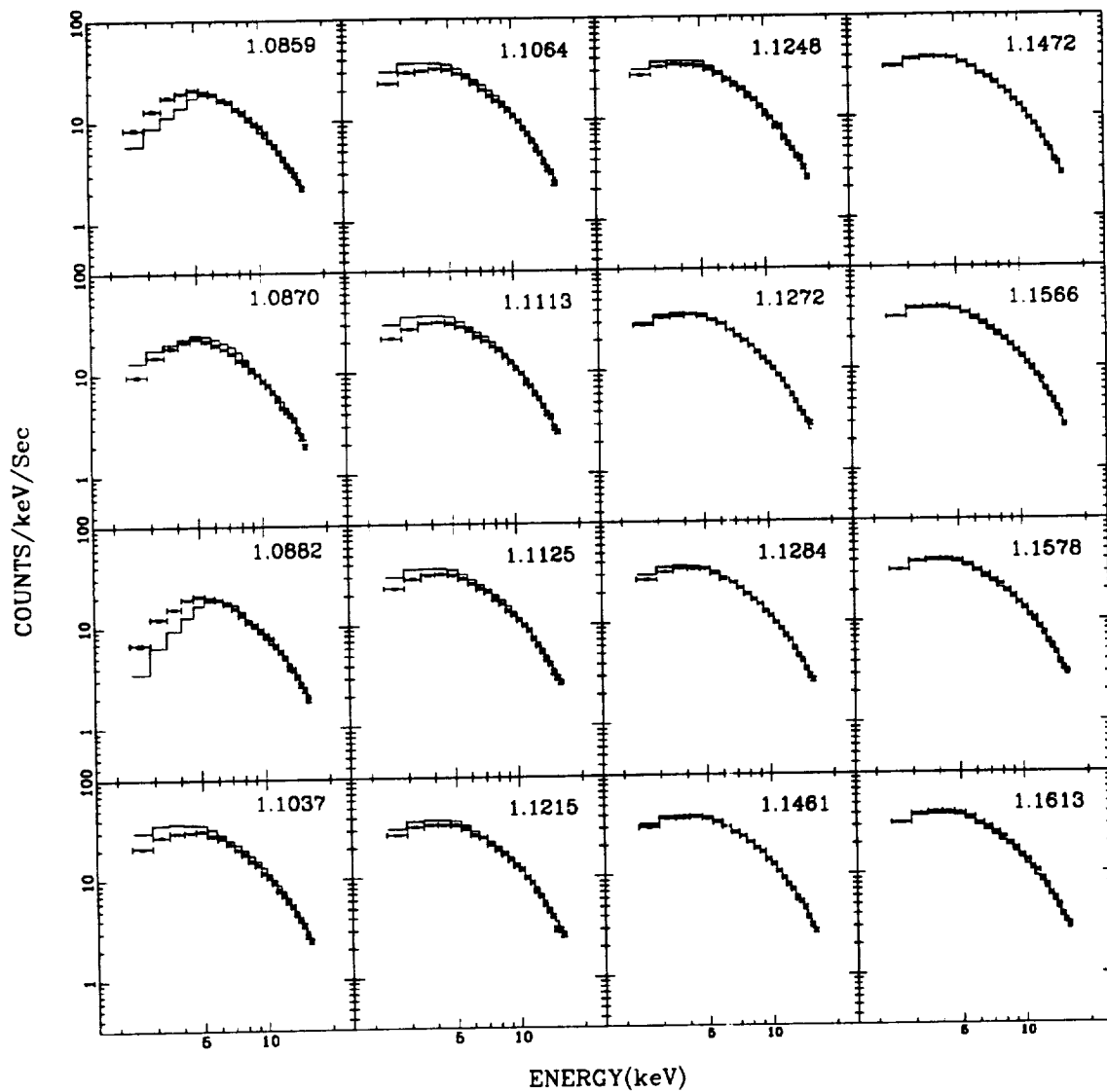
Fig. 12.— Computed PHDs for the second eclipse egress transition. The orbital phase of each PHD is indicated on the upper right-hand corner.
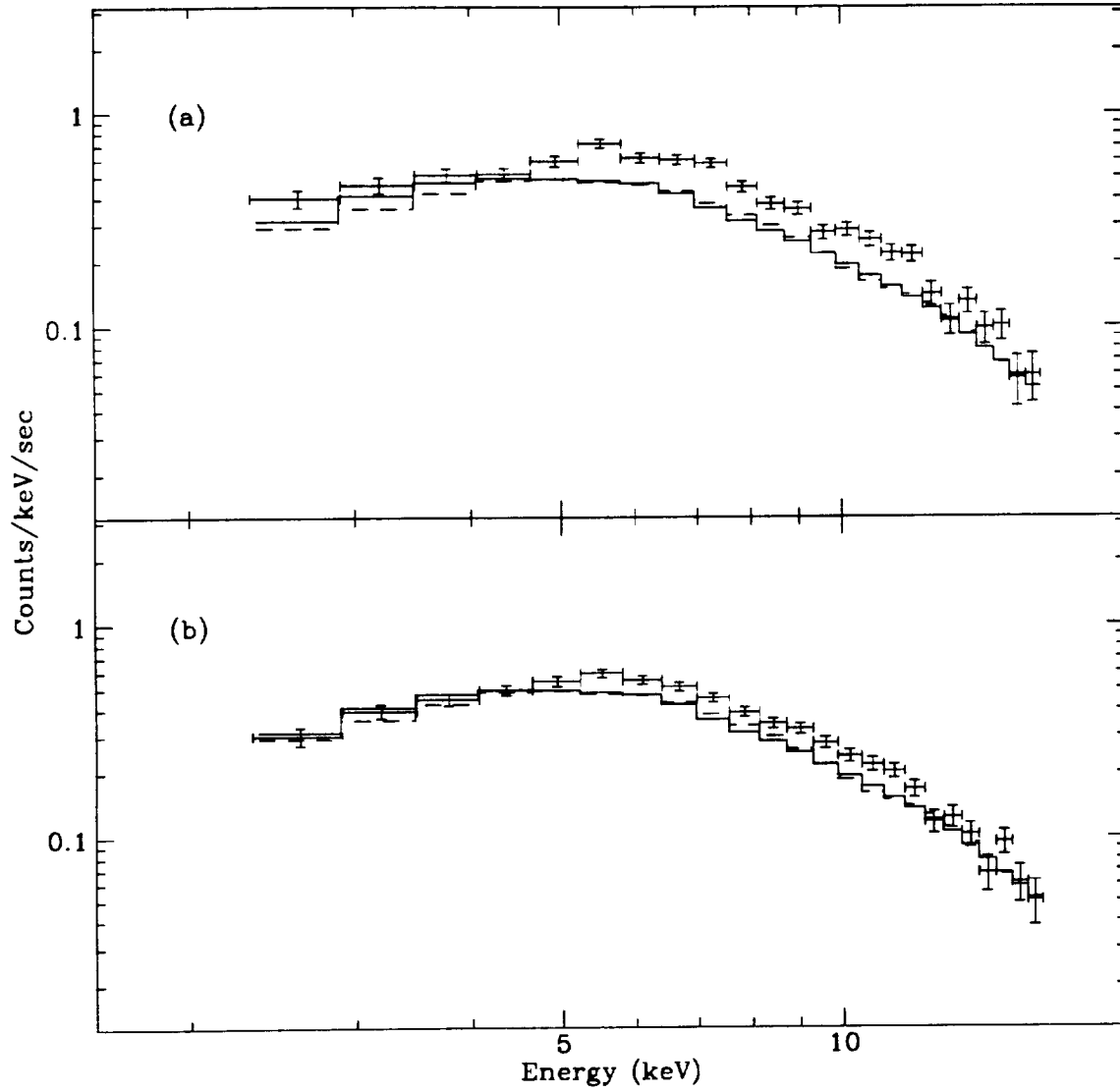
Fig. 13.— Calculated and observed PHDs of X-rays observed in eclipse. The calculated PHDs were derived from the matter distributions of the 3D hydrodynamic simulations at evolutionary times $t = 7.4$ d (dashed-line) and $t = 7.8$ d (solid-line).